Check for updates

Advanced Materials

ADVANCED MATERIALS
www.advmat.de

RESEARCH ARTICLE OPEN ACCESS

Robust Spin Splitting and Fermiology in the Layered Altermagnet $CoNb_4Se_8$

Alessandro De Vita[1,2] | Chiara Bigi[3] | Davide Romanin[4] | Matthew D. Watson[5] | Vincent Polewczyk[6] | Marta Zonno[3] | François Bertran[3] | Pietro M. Forcella[4] | My Bang Petersen[7] | Federico Motti[8] | Giovanni Vinai[8] | Manuel Tuniz[9] | Federico Cilento[10] | Mario Cuoco[11] | Brian M. Andersen[12] | Andreas Kreisel[12] | Luciano Jacopo D'Onofrio[11] | Oliver J. Clark[13] | Mark T. Edmonds[13] | Christopher Candelora[14] | Muxian Xu[14] | Siyu Cheng[14] | Alexander LaFleur[14] | Tommaso Antonelli[15] | Giorgio Sangiovanni[16] | Lorenzo Del Re[16] | Ivana Vobornik[8] | Jun Fujii[8] | Fabio Miletto Granozio[17] | Alessia Sambri[17] | Emiliano Di Gennaro[18] | Jeppe B. Jacobsen[19] | Henrik Jacobsen[20] | Iulia Cojocariu[9,10] | Marcin Szpytma[10,21] | Andrea Locatelli[10] | Tevfik Mentes[10] | Won Seop Song[22,23] | Jun Sung Kim[22,23] | Matthieu Jamet[24] | Jean-François Jacquot[24] | Pasquale Orgiani[8] | Ralph Ernstorfer[1,2] | Ilija Zeljkovic[14] | Younghun Hwang[25] | Matteo Calandra[26] | Jill A. Miwa[7] | Federico Mazzola[17,27,28]

[1]Institut für Physik und Astronomie, Technische Universität Berlin, Berlin, Germany | [2]Fritz Haber Institut der Max Planck Gesellschaft, Berlin, Germany | [3]Synchrotron SOLEIL, Saint-Aubin, France | [4]Centre de Nanosciences et de Nanotechnologies, Université Paris-Saclay, CNRS, Paris, France | [5]Diamond Light Source Ltd, Harwell Science and Innovation Campus, Didcot, UK | [6]Université Paris-Saclay, Versailles, France | [7]Department of Physics and Astronomy, Interdisciplinary Nanoscience Center, Aarhus University, Aarhus C, Denmark | [8]CNR-Istituto Officina dei Materiali (IOM), Unità di Trieste, Basovizza (TS), Italy | [9]Dipartimento di Fisica, Università degli Studi di Trieste, Trieste, Italy | [10]Elettra - Sincrotrone Trieste S.C.p.A., Trieste, Italy | [11]CNR-SPIN, Universitá di Salerno, Fisciano (SA), Italy | [12]Niels Bohr Institute, University of Copenhagen, Copenhagen, Denmark | [13]School of Physics and Astronomy, Monash University, Victoria, Australia | [14]Department of Physics, Boston College, Chestnut Hill, Massachusetts, USA | [15]ETH Zürich, Zürich, Switzerland | [16]Institute for Theoretical Physics and Astrophysics, University of Würzburg, Würzburg, Germany | [17]CNR-SPIN, Complesso di Monte S. Angelo, Napoli, Italy | [18]Physics Department, University of Napoli "Federico II", Napoli, Italy | [19]Nanoscience Center, Niels Bohr Institute, University of Copenhagen, Copenhagen, Denmark | [20]European Spallation Source ERIC - Data Management and Software Center, Kgs. Lyngby, Denmark | [21]Faculty of Physics and Applied Computer Science, AGH University of Krakow, Krakow, Poland | [22]Department of Physics, Pohang University of Science and Technology, Pohang-si, Gyeongsangbuk-do, Republic of Korea | [23]Center for Artificial Low-Dimensional Electronic Systems, Institute for Basic Science, Namgu, Pohang, Republic of Korea | [24]Univ. Grenoble Alpes, CEA, CNRS, IRIG-SPINTEC, Grenoble, France | [25]Electricity and Electronics and Semiconductor Applications, Ulsan College, Ulsan, Republic of Korea | [26]Department of Physics, University of Trento, Povo, Italy | [27]Department of Physics and Astronomy 'Galileo Galilei', University of Padova, Padova, Italy | [28]CNR-Istituto di Struttura della Materia (CNR-ISM), Trieste, Italy

Correspondence: Alessandro De Vita (devita@fhi-berlin.mpg.de) | Ilija Zeljkovic (ilija.zeljkovic@bc.edu) | Younghun Hwang (younghh@uc.ac.kr) | Matteo Calandra (m.calandrabuonaura@unitn.it) | Jill A. Miwa (miwa@phys.au.dk) | Federico Mazzola (federico.mazzola@unipd.it)

Received: 20 January 2026 | **Revised:** 28 September 2026 | **Accepted:** 30 September 2026

Keywords: angle-resolved photoemission spectroscopy | antiferromagnetism | condensed matter physics | density functional theory | electronic band structure, electronic structure, layered structure, magnetism, physics, spintronics, spin splitting, spin polarization

ABSTRACT

Altermagnetism defies conventional classifications of collinear magnetic phases, combining compensated magnetization with momentum-dependent, nonrelativistic spin splitting. While altermagnetic band splitting has been established in three-dimensional compounds such as MnTe and CrSb, layered altermagnets remain far less explored spectroscopically. Here, combining termination-resolved micro-ARPES, fine photon-energy mapping, spin-ARPES, and density functional theory, we map the three-

Alessandro De Vita, Chiara Bigi, and Davide Romanin contributed equally to this work.

This is an open access article under the terms of the Creative Commons Attribution License, which permits use, distribution and reproduction in any medium, provided the original work is properly cited.
© 2026 The Author(s). *Advanced Materials* published by Wiley-VCH GmbH

dimensional fermiology of the layered *g*-wave altermagnet $CoNb_4Se_8$, obtained by ordered Co intercalation of 2H-$NbSe_2$. We resolve the spin–split branches of the altermagnetic pairs directly in the raw photoemission spectra and, with spin-ARPES at these experimentally identified momenta, show the reversal of the spin polarization at opposite momenta and between two regions of the sample, consistent with opposite time-reversal domains, and its absence along the symmetry-protected nodal Γ–K direction. We further report a weak low-temperature anomaly near $T_0 \approx 50$–60 K, detected by magnetometry, temperature-dependent micro-ARPES, and ultrafast reflectivity, whose microscopic origin remains open. These results provide a momentum-resolved benchmark of the electronic structure of a layered altermagnet.

1 | Introduction

Altermagnetism, recognized as the third elementary type in the classification of non-relativistic spin-group symmetries, is defined by the coexistence of zero-net magnetization and the lifting of Kramers degeneracies, which lead to distinctive transport phenomena [1–8]. These degeneracies are shaped by opposite spin sublattices, interconnected through rotational symmetry in real space [9–11]. Distinct from both ferromagnetism and antiferromagnetism, this newly identified phase has sparked considerable interest, presenting new challenges for the development of spin-based technologies with potentially groundbreaking properties. The absence of net magnetization offers an advantage over conventional ferromagnetic technologies by mitigating stray magnetic fields. Simultaneously, the lifting of spin degeneracies, coupled with momentum-dependent spin-locking, facilitates efficient spin filtering. Moreover, contrary to traditional collinear antiferromagnets, altermagnets intrinsically break time-reversal symmetry, giving rise to phenomena such as the anomalous Hall effect, highlighting their potential for novel electronic applications [12–15]. This rapidly evolving field presents compelling opportunities to extend this phenomenology to two-dimensional (2D) material systems [16, 17]. 2D and thin-film altermagnets, along with their layered analogues, are particularly intriguing, envisioned as altermagnetic counterparts to graphene and graphite [18]. While significant progress has been made, the high symmetry of most 2D antiferromagnets prevents the stabilization of the altermagnetic phase [19–21] and scalable layer-by-layer synthesis methods remain scarce [22], highlighting the need for innovative approaches. Building on the prediction of altermagnetism through site-ordered cobalt intercalation of the superconducting polymorph 2H-$NbSe_2$ [18], we employ a combined theoretical and experimental approach to demonstrate its altermagnetic band splitting and spin texture. The altermagnetic ground state of $CoNb_4Se_8$ was predicted, and its A-type order determined by neutron diffraction, by Regmi et al. [18]. Dale et al. reported spin-resolved photoemission evidence for nonrelativistic spin splitting, which they distinguish from a relativistic splitting near K by its nodal structure and temperature dependence [23], and Sakhya et al. spin-integrated spectra consistent with it [24]. In both works, however, the spin–split branches are not resolved separately in the spectra and are identified through the comparison with DFT, so that the spin signal cannot be assigned to specific bulk bands from the data alone. Here, we resolve the two branches of the altermagnetic pairs directly in the raw spin-integrated data (Figure 2c–g), measure their spin polarization at these experimentally identified momenta, show that it is finite and reversing along Γ–M, where any relativistic σ_z is forbidden by symmetry, and compatible with zero along the nodal Γ–K direction, where it vanishes in the bulk, and show its reversal between two regions of the sample, consistent with time-reversal domains. Finally, we report a weak low-temperature anomaly near $T_0 \approx 50$–60 K, observed in magnetometry, in temperature-dependent micro-ARPES as a renormalization of the bandwidth, and in ultrafast reflectivity as a sign change of $\Delta R/R$. Its microscopic origin remains open.

2 | Results and Discussion

Single crystals of $CoNb_4Se_8$ were synthesized using the chemical vapour transport (CVT) method; all the data presented in the following have been acquired on samples from a single growth batch. Their composition and phases were monitored by x-ray diffraction (XRD), magnetic susceptibility, specific heat capacity, and x-ray photoelectron spectroscopy (XPS) measurements (Figures S1– S4 [25]). The crystal structure depicted in Figure 1a reveals Co-intercalated $NbSe_2$ planes, which doubles the unit cell of the system, giving a 2×2 modulation. Such a 2×2 modulation is clearly visible at room temperature, as confirmed by XRD data (Figure S1), and persists in the altermagnetic phase, as revealed by low-energy electron diffraction (LEED) (Figure 1b, and Figure S1). This confirms that the unit cell doubling is an inherent feature of the crystallographic structure. Both our bulk (XRD) and surface (LEED) diffraction probes show exclusively the 2×2 superstructure on top of the primitive 1×1 $NbSe_2$ pattern, with no detectable $\sqrt{3} \times \sqrt{3}R30°$ reflections, that is, the structural fingerprint of a $CoNb_3Se_6$-type sublattice [26–29]. Any $Co_{1/3}$-type ordered intergrowth must therefore lie below the detection limit of these probes and be structurally disordered. We can therefore rule it out as the origin of the sharp dispersive features observed throughout our (micro-)ARPES dataset, which instead arise unambiguously from a well-ordered 2×2 phase consistent with stoichiometric $CoNb_4Se_8$. Spectroscopic measurements further reveal 2×2 backfolded electronic features, whose intensity diminishes progressively from 150 K and vanishes at higher temperatures (Figures S8 and S9). This temperature dependence may originate from surface-related effects or, more trivially, from thermal broadening reducing the spectral resolution. Nevertheless, these changes do not affect the central conclusions of this study, which are drawn from bulk-sensitive observations.

Similar to other intercalated transition metal dichalcogenides (TMDs) [30], $CoNb_4Se_8$ cleaves to reveal two distinct surface terminations, each displaying markedly different electronic properties. Figure 1c,d presents schematics of these two terminations, which were experimentally distinguished using scanning tunneling microscopy (STM). The Se-terminated surface, which

15214095, 0, Downloaded from https://advanced.onlinelibrary.wiley.com/doi/10.1002/adma.75367 by Universita Di Trento, Wiley Online Library on [20/10/2026]. See the Terms and Conditions (https://onlinelibrary.wiley.com/terms-and-conditions) on Wiley Online Library for rules of use; OA articles are governed by the applicable Creative Commons License

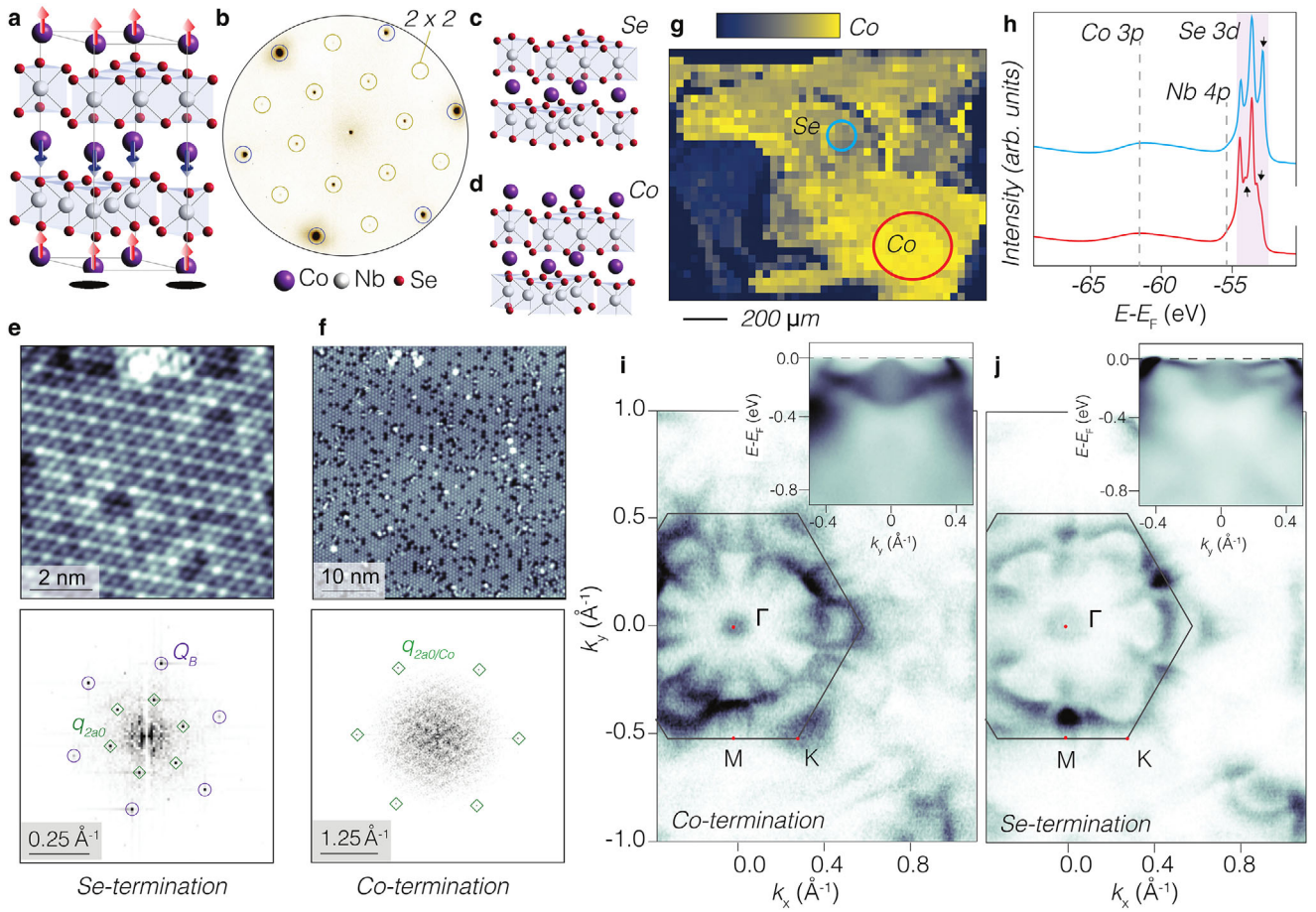


FIGURE 1 | Surface-dependent crystalline and electronic structure. (a) Schematic of $CoNb_4Se_8$ formed by 2H-$NbSe_2$ planes linked by Co atoms in a 2×2 reconstruction. (b) LEED data (25 eV, ~ 120 K) showing the 2×2 reconstruction: the orange circles indicate the 2×2 features, while the blue circles are the primitive ones. (c–d) Schematics showing the possible surface terminations (Se and Co) after cleaving. (e) Se-termination (characterized by triangular tiling) and (f) Co-termination, measured by STM, and their corresponding Fourier transforms. (g) micro-ARPES spatial map acquired by measuring the Se 3d and Co 3p core levels; yellow corresponds to Co-terminated regions. (h) Core levels acquired from the two different surface terminations [curve colors matching the circle colors in (g)]; the highlighted spectral features are attributed to surface replicas for the Co-termination. (i–j) Corresponding Fermi surfaces and (E, k) dispersions, collected at 25 K with p-polarized photons at 47.5 eV (black indicates high intensity in the ARPES scale).

appears to be the cleanest, exhibits the characteristic triangular tiling of the 2H-$NbSe_2$ polymorph (Figure 1e). In contrast, the Co-terminated surface is typically more disordered yet remains clearly distinguishable from the Se-terminated surface (Figure 1f). Additional STM data are provided in Figure S3.

We used angle-resolved photoelectron spectroscopy with few-micron spatial resolution (micro-ARPES) to validate these observations. Fermi surfaces for each surface termination were acquired by mapping the surface composition through Se 3d and Co 3p core level measurements (Figure 1g). Spatially resolved maps indicate that each homogeneously terminated region spans approximately 20 μm laterally. According to our data in Figure 1h, the Se-termination (blue curve) exhibits surface replicas of the 3d core levels, whereas Co-terminated regions (red curve) show distinct spectral features, including an additional peak at lower energies possibly formed by a different coordination of Co-Se atoms. It is important to note that the cleaving process can introduce random surface vacancies, which are readily identifiable in the core level spectra and may locally degrade the ARPES signal. In any case, the altermagnetic phenomena discussed here are of bulk origin and remain unaffected by either surface terminations or surface disorder.

The Fermi surface maps, along with the energy and momentum (E, k) dispersions along the Γ – M direction (Figure 1i,j; black indicates the presence of electrons), reveal a complex and rich electronic structure. For both terminations, the intensity displays a pronounced threefold symmetry, accompanied by multiple petals and back-folded features. As shown Figure S8, such a modulation is evidenced by the replication of Γ-point features at the M-point. The Co-termination is overall the most prevalent and dominates high-resolution ARPES measurements with larger light spot sizes, as seen in Figure S6– S12. In any case, our study reveals a bulk phenomenology, thus terminations do not affect the results we present. For simplicity, we accordingly restrict our analysis to data obtained from this termination and we move to the characterization of the magnetic phase.

15214095, 0, Downloaded from https://advanced.onlinelibrary.wiley.com/doi/10.1002/adma.75367 by Universita Di Trento, Wiley Online Library on [20/10/2026]. See the Terms and Conditions (https://onlinelibrary.wiley.com/terms-and-conditions) on Wiley Online Library for rules of use; OA articles are governed by the applicable Creative Commons License

$CoNb_4Se_8$ crystallizes in the centrosymmetric space group $P6_3/mmc$, No. 194. The A-type collinear antiferromagnetic order along c reduces the magnetic space group to $P6'_3/m'm'c$, and the corresponding non-relativistic spin space group is generated by combining the crystallographic operations of 6/mmm with the spin operations that relate the two opposite-spin Co sublattices, in agreement with the spin-group assignments of Refs. [9, 5, 31] for this class of compounds, and with the symmetry analyses recently reported on the same compound [23, 26]. Operations that preserve the Co sublattices (the threefold rotations, inversion, the mirrors perpendicular to ⟨100⟩ and the twofold axes along ⟨100⟩) are combined with the identity in spin space, whereas those that exchange them (the $\{6_{001}|00\frac{1}{2}\}$ screw, the mirror $\{m_{001}|00\frac{1}{2}\}$, the c glides perpendicular to $\langle 1\bar{1}0\rangle$ and the twofold axes along $\langle 1\bar{1}0\rangle$) are combined with a spin flip. In Litvin notation the spin space group is $P^{-1}6_3/^{-1}m\ ^1m\ ^{-1}c\ ^{\infty m}1$, the same as for the NiAs-type altermagnets MnTe and CrSb [9, 10, 32]; the full analysis is given in Supporting Information, Section VI and Table S3 [33–35]. From the general classification of space groups and their associated allowed altermagnetic spin-splittings [31], it follows that the lowest-order non-relativistic spin–split form factor compatible with the spin group of 2×2 reconstructed $CoNb_4Se_8$ is the g-wave harmonic

$$\Delta_s(\mathbf{k}) \propto k_z\, k_y\, (3k_x^2 - k_y^2), \tag{1}$$

whose nodal manifold consists of the two high-symmetry planes $k_z = 0$ and $k_z = \pi/c$ together with the three vertical mirror planes containing the Γ–K high-symmetry lines. The splitting therefore vanishes in the $k_z = 0$ and $k_z = \pi/c$ planes (as required by the antiferromagnetic Kramers degeneracy at those planes) and along the directions where the angular factor $k_y(3k_x^2 - k_y^2)$ is zero, while it reaches its maximum at intermediate k_z (such as $k_z = \pi/2c$) and at general k-points off the high-symmetry directions. The role of k_z is thus pivotal: the breakdown of Kramers degeneracy manifests in the electronic structure away from bulk high-symmetry points. Photon-energy-dependent measurements are therefore required to select k_z, and fine photon-energy steps are used to tune the photoemission matrix elements and to select favorable k_z windows. The large c-axis lattice constant of $CoNb_4Se_8$ (see Figure S1 and discussion) means each photon energy probes multiple k_z values simultaneously, leading to partial spectral broadening [36]. Nevertheless, varying photon energy enables modulation of matrix elements and band intensities, which significantly enhances the detection of subtle spectral features. This capability is exemplified in the Fermi surface maps obtained at different photon energies in Figure 2a–c (see also Figures S10– S12, where photon energy measurements with fine step are reported). Owing to the large c axis, each photon energy integrates over a k_z window ($\Delta k_z \approx 0.2$ Å^{-1}) comparable to the Γ–A distance ($\pi/c \approx 0.25$ Å^{-1}); the maps in Figure 2a–c are centered near bulk Γ, near A and at an intermediate k_z, respectively. The nodal structure is therefore identified through spin-resolved observables that are independent of k_z (the null along Γ–K) or protected by symmetry against k_z broadening (the reversal at opposite momenta; Supporting Information, Section VIII).

While all Fermi surfaces share common features, that is, hexagonal flower-like central contours and elongated "spindles", the map in Figure 2c reveals a clear splitting in the electronic band structure, which complements and refines the picture emerging from prior ARPES work on the same compound [23, 24]. In particular, the altermagnetic splitting is directly visible in our raw spin-integrated photoemission data, as resolved contours in the Fermi-surface maps at intermediate k_z (Figure 2c, also highlighted by arrows in Figure 2d), and as two distinct peaks in the corresponding momentum distribution curves (MDCs) at the Fermi level (Figure 2g). The combination of micro-ARPES with a $\sim 4\,\mu$m beam spot, fine photon-energy mapping in the range from 25 to 75 eV, and systematic light-polarization control further allows us to address individual single-termination regions, select favorable k_z windows in which the g-wave splitting is symmetry-allowed, and tune the photoemission matrix elements so that the otherwise nearly degenerate branches become unambiguously visible.

We note that in the Fermi surfaces, some of the spectral features appear as filled patches of intensity rather than contours as expected from density functional theory (DFT) calculations. This is attributable to photoemission matrix elements, which strongly vary with both geometry and photon energy. For the same reason, matrix element effects cause the splitting to be more or less evident at nominally the same $k_z = \pi/2c$, but different photon energies.

The experimental Fermi surfaces align with DFT (Figure 2f and Figure S13) in capturing the fermiology across the k_z planes. The spin-splitting of the Kramers-paired bands at multiple momenta show remarkable agreement. This agreement is further highlighted in Figure 2d, where the spin-up (red) and spin-down (blue) bands from the DFT calculations coincide exactly with the experimental data. There is a similarly strong match between the DFT calculated (E, k) distributions across different k_z values and acquired micro-ARPES data, as shown in Figure 2h, where blue and orange curves correspond to Γ and A points, respectively (see also Figure S14 for DFT-calculated (E, k) spectra in the Γ–K direction). In order to display a simpler representation of the electronic dispersion for comparison with micro-ARPES measurements, we have mapped the spin-polarized electronic eigenvalues and eigenvectors of the bulk altermagnetic 2×2 $CoNb_4Se_8$ supercell (SC) into the bigger Brillouin zone of the 1×1 $NbSe_2$ primitive cell (PC) via an unfolding scheme [37]. The thickness of the bands in the unfolded electronic dispersions is proportional to the spectral weight

$$P_{\vec{K}m}(\vec{k}_i) = \sum_n \left| \langle \vec{K}m \rangle\, \vec{k}_i n \right|^2, \tag{2}$$

which is the probability of finding a set of PC states, $|\vec{k}_i n\rangle$, contributing to the SC state, $|\vec{K}m\rangle$ [37], where m and n are band indices and i runs over the number of $\vec{K}$ vectors.

Notably, while eigenvalues for $k_z = 0$ and $k_z = \pi/c$ are spin-degenerate (as expected for an antiferromagnetic system), DFT results for $k_z = \pi/2c$ (rightmost panel in Figure 2h, where the red/blue colors are used to highlight spin-up/down bands) provide a precise benchmark for finding where Kramers degeneracies are lifted, identifying $CoNb_4Se_8$ as a g-wave altermagnet and enabling a one-to-one correspondence with the experimental data. Near the Fermi level, the theoretical altermagnetic splitting

15214095, 0, Downloaded from https://advanced.onlinelibrary.wiley.com/doi/10.1002/adma.75367 by Universita Di Trento, Wiley Online Library on [20/10/2026]. See the Terms and Conditions (https://onlinelibrary.wiley.com/terms-and-conditions) on Wiley Online Library for rules of use; OA articles are governed by the applicable Creative Commons License

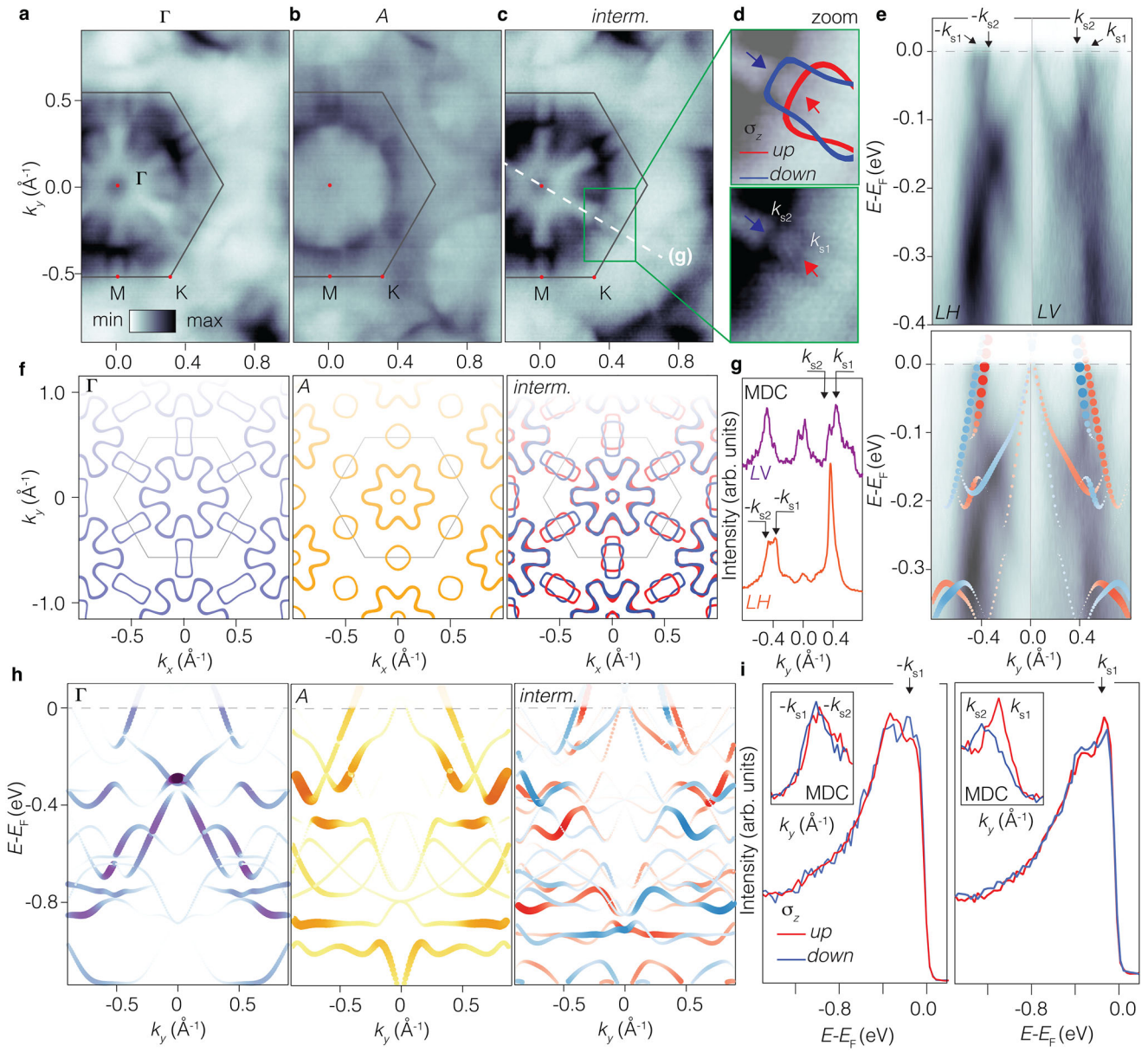


FIGURE 2 | Fermiology, DFT, and spin splitting. Fermi surfaces at bulk Γ (51 eV, (a)), A (75 eV, (b)), and an intermediate point near $k_z = \pi/2c$ (55 eV, (c)). (d) Zoom-in on the splitting, with and without DFT calculations. The arrows indicate sections where the bands are prominently separated. (e) *Top*: (E, k)-spectra at 44 eV (nominal k_z near A; see Supporting Information, Section VIII), where matrix elements favor the split branches (see Supporting Information for additional energies), using *p*- (LH, left) and *s*-polarized (LV, right) light. *Bottom*: same (E, k)-spectra with overlaid DFT calculations. (f) DFT spin-polarized 2D Fermi surfaces of $CoNb_4Se_8$ at $k_z = 0$, $k_z = \pi/c$, and $k_z = \pi/2c$. (g) MDCs at the Fermi level from (e), highlighting multiple split bands. (h) DFT spin-polarized bands of $CoNb_4Se_8$ unfolded in the large Brillouin zone of (1×1) $NbSe_2$ along $M - \Gamma - M$ for $k_z = 0$, $k_z = \pi/c$, and $k_z = \pi/2c$, with spectral weight $P_{\vec{K}m}$ defined in Equation (2). (i) spin-ARPES at opposite *k*-points (55 eV *p*-polarized, as in (c)), showing EDCs at k_{s1} and MDCs at the Fermi level (insets).

is in excellent agreement with the experimental spectra (lower panel in Figure 2e), and the bands forming the altermagnetic pairs are labeled as $\pm k_{s1,s2}$. Including spin–orbit coupling (SOC) opens gaps of up to 0.1 and 0.2 eV at band crossings at Γ and A, respectively, where the altermagnetic splitting vanishes by symmetry. At the momenta of the altermagnetic pairs $\pm k_{s1,s2}$, SOC shifts the bands by less than 20 meV and leaves $\langle S_z \rangle \approx \pm 0.5\hbar$ (essentially fully polarized), whereas the nonrelativistic splitting is ≈ 150 meV (Supporting Information, Section VI and Table S4). Moreover, any time-reversal-even σ_z, including the hidden Ising polarization of the $NbSe_2$ layers [38, 39], is forbidden along Γ–M by the vertical mirror containing this direction, and cannot account for the spin-ARPES pattern discussed below. The non-zero spin character of these bands is further validated by spin-ARPES measurements (Figure 2i), collected for the σ_z spin component at multiple *k* values within the plane centered at $k_z = \pi/2c$. Both energy distribution curves (EDCs) at $\pm k_{s1}$ and MDCs at the Fermi level across numerous *k* points reveal a small, yet clear, spin-reversal pattern. The corresponding spin polarization and its 1σ statistical error bands are shown in Figure S23, to directly assess the significance of the sign reversal. The antisymmetric part of the polarization, $[P(k) -$

15214095, 0, Downloaded from https://advanced.onlinelibrary.wiley.com/doi/10.1002/adma.75367 by Universita Di Trento, Wiley Online Library on [20/10/2026]. See the Terms and Conditions (https://onlinelibrary.wiley.com/terms-and-conditions) on Wiley Online Library for rules of use; OA articles are governed by the applicable Creative Commons License

$P(-k)]/2 \approx 6 \pm 1.5\%$ in magnitude at $E - E_F \approx -0.05$ eV, corresponds to about four standard deviations and is insensitive by construction to any k-independent instrumental offset; the data treatment is detailed in Supporting Information, Section VII. This behavior is consistent with theoretical predictions and is observed at four different k points in the MDCs (insets of Figure 2i), further supporting the validity of our findings. Importantly, a non-zero spin signal and sign swap at time-reversal momenta have been found systematically for various cleaves. Moreover, moving the beam spot by ≈ 1 mm on the same cleaved surface reverses the spin contrast at the same momentum, consistent with a region of opposite time-reversal domain (Figure S20). An additional sanity check is provided by spin-ARPES along the Γ–K direction, which corresponds to a symmetry-protected nodal plane of the g-wave form factor of Equation (1): the measured spin signal along this direction is compatible with zero within the 1σ uncertainty (Figures S19 and S23). In the bulk, σ_z along Γ–K vanishes by symmetry even when SOC is included, because the c glide containing Γ–K is a symmetry of $P6'_3/m'm'c$ without time reversal; at the surface this glide is lost, but the hidden Ising polarization of the topmost $NbSe_2$ layer that would then be allowed is expected to be strongly reduced by the covalent bonding of adjacent layers through the intercalated Co (Supporting Information, Section VII). This discussion, along with considerations about the domain size and extra sets of data, is expanded in the dedicated Section VII of the Supporting Information and Figures S19– S23. The combination of micro-ARPES and spin-ARPES presented here thus robustly confirms the altermagnetic character of $CoNb_4Se_8$, in excellent agreement with DFT calculations showing the g-wave altermagnetic splitting and its k_z dependence.

Interestingly, we observe a small kink at $T \approx 50$ K in the magnetization as measured by SQUID (Figure S3), which we refer to as the low-temperature anomaly at T_0. We note that this temperature does not coincide with the ~ 28–36 K transition recently associated with the non-centrosymmetric $\sqrt{3} \times \sqrt{3} R30°$ ordering of Co-excess $CoNb_3Se_6$ [18, 26, 27, 40], which is not detected in our diffraction probes (Figure S1). Moreover, due to competing magnetic interactions, even small changes in the Co concentration would stabilize a magnetic transition temperature lower than 170 K [26], which is inconsistent with our data. Therefore, the presence of this signal does not change the robustness of the conclusions presented above; however, it warrants further investigation. In order to gain more insight into this phenomenon, we measured micro-ARPES spectra below and above T_0 at two photon energies and at linear vertical (LV) and linear horizontal (LH) light polarizations. We report a temperature-driven behavior (Figure 3a), with a significant band renormalization (Figure 3a–d and Figure S7). We observe the renormalization across multiple photon energies and independently of light polarization; in particular, Figure 3c displays the difference in spectral intensity between data collected above and below T_0 for the different photon energies and polarizations, so that modifications to the bandwidth appear more evidently. This is also shown more explicitly in Figure 3d with EDCs extracted at specific k points (indicated in Figure 3a) across various photon energies for both temperatures. Crucially, micro-ARPES provides precise spatial control, allowing us to maintain the same position when varying the temperature.

Additionally, we performed time-resolved reflectivity measurements on the same batch of samples. Figure 3e shows the evolution of the reflectivity variation ($\Delta R/R$) measured shortly after the absorption of the pump pulse ($t - t_0 \sim 100$ fs). At a fluence of $\approx 150\ \mu$J cm^{-2}, two distinct sign changes in the $\Delta R/R$ signal are observed near 130 and 50 K, as measured directly by the cryostat sensor, corresponding to ~ 170 K and ~ 60 K on the sample due to nonlinear sensor-to-sample offset. A sign change of $\Delta R/R$ is commonly observed when the electronic structure changes at the onset of an ordered phase, as in cuprate superconductors and charge–density–wave systems [41, 42]. The sign change near 130 K can be related to the paramagnetic-altermagnetic transition; the effect near 50 K coincides with the band renormalization shown in the micro-ARPES spectra in Figure 3 and with the kink in the magnetization. The microscopic origin of this anomaly remains open, and extrinsic effects cannot be excluded. We only note that the optical response is electronic in character: as detailed in the Supporting Information, Section IV, the steady-state pump-induced heating is below 3 K, and the reflectivity signal $\Delta R/R$ (650 nm) evolves on a sub-200 fs timescale, faster than expected for phonon-mediated effects. This statement concerns the probe signal and not the origin of the anomaly: the sign change reflects a modification of the allowed optical transitions, consistent with the band renormalization observed by micro-ARPES. No anomaly is resolved in the heat capacity near T_0 (Supporting Information, Section I); given the dominant lattice contribution at these temperatures, this does not exclude a small electronic contribution, and high-resolution thermodynamic measurements will be required to establish the origin of the anomaly.

3 | Conclusions

In conclusion, we have resolved the altermagnetic band splitting of the layered g-wave altermagnet $CoNb_4Se_8$, stabilized via Co intercalation in 2H-$NbSe_2$. Using micro-ARPES, spin-ARPES, and temperature-dependent reflectivity combined with DFT, we provide direct evidence of Kramers degeneracy lifting and reveal the spin-polarized band splitting characteristic of altermagnetic phenomena; moreover, we report a low-temperature anomaly accompanied by a renormalization of the bandwidth with temperature, whose microscopic origin requires further investigation. These findings establish $CoNb_4Se_8$ as a well-characterized model system for layered altermagnets, on which future studies of exfoliated flakes, heterostructures and transport can build.

4 | Methods

4.1 | Sample Growth

Single crystals of $CoNb_4Se_8$ were synthesized using the chemical vapor transport (CVT) method. High-purity cobalt (Co, 99.99%), niobium (Nb, 99.999%), and selenium (Se, 99.9999%) powders served as starting materials. To prevent contamination and residual oxygen during synthesis, the quartz ampoule was chemically cleaned and subjected to vacuum heat treatment prior to loading. The raw materials were then sealed in a quartz ampoule (approximately 10 mm in diameter and 150 mm in length) along with iodine (5 mg/cm^3 relative to ampoule volume) as the transport

15214095, 0, Downloaded from https://advanced.onlinelibrary.wiley.com/doi/10.1002/adma.75367 by Universita Di Trento, Wiley Online Library on [20/10/2026]. See the Terms and Conditions (https://onlinelibrary.wiley.com/terms-and-conditions) on Wiley Online Library for rules of use; OA articles are governed by the applicable Creative Commons License

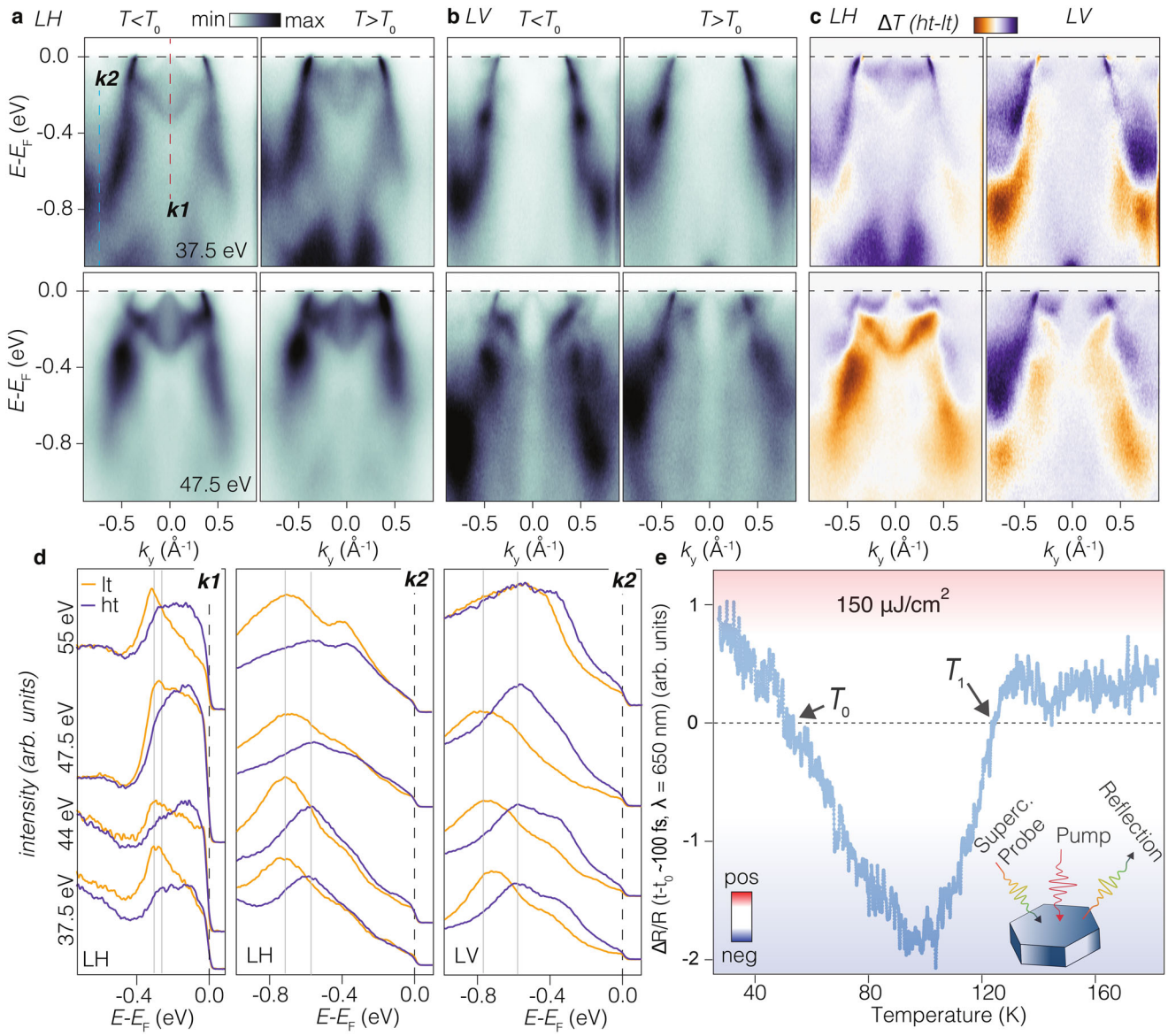


FIGURE 3 | Low-temperature anomaly. ARPES spectra (black indicates high intensity in the ARPES scale) collected at two distinct photon energies: 37.5 eV (top row) and 47.5 eV (bottom row), and for temperatures above and below T_0. These are shown for both (a) *p*-polarization (LH) and (b) *s*-polarization (LV). (c) Difference between spectra collected above and below T_0; orange (purple) corresponds to a negative (positive) difference. The strong electronic renormalization manifests as a decrease in the overall bandwidth, while k_F remains constant. (d) EDCs collected at different photon energies (indicated along the vertical axis) for spectra below T_0 (orange) and above it (purple). These are shown for two k values (k_1 and k_2) as indicated in (a). (e) $\Delta R/R$ signal as measured by ultrafast reflectivity at $t - t_0 \sim 100$ fs for 150 μJ cm^{-2} fluence. The two zero-crossings of the $\Delta R/R$ signal at $T_0 \approx 50$ K and $T_1 \approx 130$ K are highlighted. The temperature axis refers to the sensor; on the sample, T_0 corresponds to ~ 60 K and T_1 corresponds to ~ 170 K.

agent. The sealed ampoule was evacuated to a high vacuum and placed in a two-zone horizontal furnace, with the source region maintained at a higher temperature than the growth region. Optimal temperature gradients and iodine concentration were critical for achieving high-quality crystal growth. For $CoNb_4Se_8$, the source region was held at 960°C–980°C, while the growth region temperature was initially increased incrementally from 880°C to 900°C over 100 h. Subsequently, both zones were held at constant temperatures for an additional 300 h to facilitate the growth of large single crystals. Finally, the temperature was reduced gradually over 100 h, with the source region cooled to 200°C and the growth region to 100°C, before allowing the ampoule to cool naturally to room temperature. The resulting single crystals measured approximately $5 \times 5 \times 0.1$ mm^3. Residual iodine was removed from the crystals by rinsing with a methanol solution. The mole fraction "x" in Co_xNbSe_2 was preliminarily determined using energy-dispersive x-ray spectroscopy (EDS) in a field-emission scanning electron microscope (FE-SEM, JEOL 7500). High-precision quantification was subsequently performed using x-ray photoelectron spectroscopy (XPS) at the APE-HE beamline of the Elettra synchrotron radiation facility in Trieste, Italy (details in Supporting Information). The crystal structure and quality were confirmed using high-resolution x-ray diffraction (XRD, D8 Advance, Bruker, Germany). Additional

15214095, 0, Downloaded from https://advanced.onlinelibrary.wiley.com/doi/10.1002/adma.75367 by Universita Di Trento, Wiley Online Library on [20/10/2026]. See the Terms and Conditions (https://onlinelibrary.wiley.com/terms-and-conditions) on Wiley Online Library for rules of use; OA articles are governed by the applicable Creative Commons License

sample characterization is shown in Sections I and II of the Supporting Information.

4.2 | Synchrotron Radiation Measurements

Micro-ARPES measurements were performed on in situ cleaved samples. The beam was focused using the capillary mirror optic at the I05 beamline at Diamond Light Source, with a final beam spot of $\sim 4\,\mu$m FWHM. The base sample temperature was 25 K. The standard ARPES data were acquired at the CASSIOPEE beamline at Synchrotron SOLEIL (Paris, France) with momentum and energy resolutions better than 0.018 $Å^{-1}$ and 10 meV, respectively. The sample temperature was fixed at circa 20 K, that is, well below the magnetic transition temperature, for all measurements. The Fermi surfaces were obtained by rotating the sample around the analyzer focus, with the slit positioned orthogonal to the rotation axis. Data were acquired using photon energies in the range from 25 to 75 eV, which allows us to tune the photoemission matrix elements and to locate the high-symmetry points along k_z (Supporting Information, Section VIII). Spin-ARPES was performed using V-LEED technology at the APE-LE laboratory at the Elettra Synchrotron (Trieste, Italy) and with LH light. For these measurements, the samples were aligned with the slit along the Γ–M direction and kept under normal emission conditions. The various momenta were reached via the use of deflectors. The spin-ARPES was performed with the sample held at a temperature of 15 K. The treatment of the spin-resolved data is described in Supporting Information, Section VII. In all ARPES and spin-ARPES measurements, the samples were fixed to the sample holder using silver epoxy (HD20E, Epotek). A small ceramic post was secured to the top of the sample using the same epoxy. Once the samples were introduced into the measurement chamber, they were cleaved under ultrahigh vacuum conditions (better than 10^{-10} mbar) and after being cooled to the base temperature of 15 K.

4.3 | Computational Details

Collinear spin-polarized DFT calculations (without Hubbard correction, that is, DFT+U) have been performed using the plane-wave pseudopotential method as implemented in the Quantum ESPRESSO package v.7.2 [43, 44]. We employed a norm-conserving pseudopotential for Se atoms and ultrasoft pseudopotentials for Nb and Co atoms, the latter taken from the Garrity–Bennett–Rabe–Vanderbilt library [45], with energy cutoffs of 45 and 450 Ry for the wave function and electron density, respectively. Electronic band structure and energetics have been obtained using the Perdew–Burke–Ernzerhof (PBE) [46] exchange-correlation functional. The Brillouin zone has been sampled with a Γ-centered Monkhorst–Pack k-point mesh of $9 \times 9 \times 16$ points and a first-order Methfessel–Paxton [47] electronic smearing of 5 mRy, ensuring convergence of the total energy per atom in the supercell within 1 meV/atom. We investigated the energetics of Co-intercalated 2×2 $NbSe_2$ ($CoNb_4Se_8$) in the paramagnetic (PM), ferromagnetic (FM), and altermagnetic (ALM) configurations and as a function of the Co position by relaxing both lattice parameters and internal coordinates until residual forces were below 10^{-3} Ry/Bohr (see Supporting Information, Section VI). Bulk altermagnetic 2×2 $CoNb_4Se_8$ supercell eigenvalues and eigenvectors have then been mapped into the 1×1 $NbSe_2$ primitive-cell Brillouin zone using the scheme of Popescu and Zunger [37], as implemented in the code `unfold.x` [48].

Author Contributions

F.M. and M.C. coordinated the project. F.M., A.D.V., M.C., D.R., J.A.M, and I.Z. wrote the manuscript with input from all authors. F.M., A.D.V., C.B., M.D.W., F.B., O.J.C, J.A.M., I.V., J.F., M.Z., M.B.P., and J.B.J. performed the ARPES measurements. F.Mo. and G.V. performed high-resolution XPS measurements. F.C. and M.T. performed the optical spectroscopy, M.C. and D.R. performed the DFT calculations, I.Z., C.C., M. X., S.C., and A.L. performed the STM measurements, and Y.H. synthesized the crystals, performed the resistivity, and initial characterization. W.S.S. and J.S.K. performed and analyzed the heat-capacity measurements. All authors contributed to the discussion of the work.

Acknowledgments

F.M. greatly acknowledges the NFFA-DI funded by the European Union – NextGenerationEU, M4C2, within the PNRR project NFFA-DI, Grants No. CUP B53C22004310006 and No. IR0000015, and MUR funding within the FIS2 (n. 1236, 1-8-2023) Project no. FIS-2023-03652 (CUP D53C25001950001). A.D.V. acknowledges funding from the Deutsche Forschungsgemeinschaft (DFG) within Transregio TRR 227 Ultrafast Spin Dynamics project B07, the Max Planck Society, and BERLIN QUANTUM, an initiative endowed by the Innovation Promotion Fund of the city of Berlin. D.R. acknowledges support from the HPC resources of IDRIS, CINES, and TGCC under Allocation No. 2024-A0160914101 made by GENCI. M.B.P. and J.A.M gratefully acknowledge support from the Danish Agency for Science and Higher Education (DanScatt Grant No. 7129-00018B). M.C. acknowledges the European Union (ERC, DELIGHT, 101052708). I.Z. gratefully acknowledges the support from the US Department of Energy grant number DE-SC0025005. We thank A. Jones for his support during measurements at the SGM4 beamline. This work was partially performed in the framework of the Nanoscience Foundry and Fine Analysis (NFFA-MUR Italy Progetti Internazionali) project. F. Motti acknowledges the support of the EC project SINFONIA (Grant No. H2020-FET-OPEN-964396). This work was supported by the National Research Foundation of Korea (NRF) funded by the Ministry of Education, Science and Technology (Grants No. NRF-2019M2C8A1057099 and No. NRF-2022R1I1A1A01063507). J.S.K. was supported by the Institute for Basic Science (IBS) through the Center for Artificial Low-Dimensional Electronic Systems (IBS-R014-D1). Y.H.H. was supported by the National Research Foundation of Korea (NRF) grant funded by the Korean government (MSIT) (RS-2025-24742993). The authors gratefully thank Prof. I. Mazin and Prof. N.J. Ghimire for useful insights and discussion.

Open access funding enabled and organized by Projekt DEAL.

Conflicts of Interest

The authors declare no conflicts of interest.

Data Availability Statement

The data that support the findings of this study are available from the corresponding authors upon reasonable request. The code that support the findings of the study is available from the corresponding authors on reasonable request.

References

1. L. Bai, W. Feng, S. Liu, L. Šmejkal, Y. Mokrousov, and Y. Yao, "Altermagnetism: Exploring New Frontiers in Magnetism and Spintronics," *Advanced Functional Materials* 34, no. 49 (2024): 2409327.

15214095, 0, Downloaded from https://advanced.onlinelibrary.wiley.com/doi/10.1002/adma.75367 by Universita Di Trento, Wiley Online Library on [20/10/2026]. See the Terms and Conditions (https://onlinelibrary.wiley.com/terms-and-conditions) on Wiley Online Library for rules of use; OA articles are governed by the applicable Creative Commons License

2. T. A. Maier and S. Okamoto, "Weak-Coupling Theory of Neutron Scattering as a Probe of Altermagnetism," *Physical Review B* 108 (2023): L100402.

3. T. Jungwirth, R. M. Fernandes, J. Sinova, and L. Šmejkal, "Altermagnets and Beyond: Nodal Magnetically-Ordered Phases," preprint, arXiv, September 16, 2024, arXiv:2409.10034.

4. C. Song, H. Bai, Z. Zhou, et al., "Altermagnets as a New Class of Functional Materials," *Nature Reviews Materials* 10 (2025): 473–485.

5. L. Šmejkal, J. Sinova, and T. Jungwirth, "Emerging Research Landscape of Altermagnetism," *Physical Review X* 12 (2022): 040501.

6. I. Mazin, K. Koepernik, M. D. Johannes, R. González-Hernández, and L. Šmejkal, "Prediction of Unconventional Magnetism in Doped $FeSb_2$," *Proceedings of the National Academy of Sciences* 118, no. 42 (2021): e2108924118.

7. I. Mazin, "Editorial: Altermagnetism – A New Punch Line of Fundamental Magnetism," *Physical Review X* 12 (2022): 040002.

8. H. Reichlova, R. Lopes Seeger, R. González-Hernández, et al., "Observation of a Spontaneous Anomalous Hall Response in the Mn_5Si_3 d-Wave Altermagnet Candidate," *Nature Communications* 15 (2024): 4961.

9. L. Šmejkal, J. Sinova, and T. Jungwirth, "Beyond Conventional Ferromagnetism and Antiferromagnetism: A Phase With Nonrelativistic Spin and Crystal Rotation Symmetry," *Physical Review X* 12 (2022): 031042.

10. J. Krempaský, L. Šmejkal, S. W. D'Souza, et al., "Altermagnetic Lifting of Kramers Spin Degeneracy," *Nature* 626, no. 7999 (2024): 517–522.

11. L.-D. Yuan and A. Zunger, "Degeneracy Removal of Spin Bands in Collinear Antiferromagnets with Non-Interconvertible Spin-Structure Motif Pair," *Advanced Materials* 35, no. 31 (2023): 2211966.

12. O. Fedchenko, J. Minár, A. Akashdeep, et al., "Observation of Time-Reversal Symmetry Breaking in the Band Structure of Altermagnetic RuO_2," *Science Advances* 10, no. 5 (2024): eadj4883.

13. L. Šmejkal, R. González-Hernández, T. Jungwirth, and J. Sinova, "Crystal Time-Reversal Symmetry Breaking and Spontaneous Hall Effect in Collinear Antiferromagnets," *Science Advances* 6, no. 23 (2020): eaaz8809.

14. Z. Feng, X. Zhou, L. Šmejkal, et al., "An Anomalous Hall Effect in Altermagnetic Ruthenium Dioxide," *Nature Electronics* 5, no. 11 (2022): 735–743.

15. R. D. Gonzalez Betancourt, J. Zubáč, R. Gonzalez-Hernandez, et al., "Spontaneous Anomalous Hall Effect Arising From an Unconventional Compensated Magnetic Phase in a Semiconductor," *Physical Review Letters* 130 (2023): 036702.

16. S. Zeng and Y.-J. Zhao, "Description of Two-Dimensional Altermagnetism: Categorization Using Spin Group Theory," *Physical Review B* 110 (2024): 054406.

17. I. Mazin, R. González-Hernández, and L. Šmejkal, "Induced Monolayer Altermagnetism in $MnP(S,Se)_3$ and FeSe," preprint, arXiv, September 5, 2023, arXiv:2309.02355.

18. R. B. Regmi, H. Bhandari, B. Thapa, et al., "Altermagnetism in the Layered Intercalated Transition Metal Dichalcogenide $CoNb_4Se_8$," *Nature Communications* 16 (2025): 4399.

19. C. Autieri, G. Cuono, C. Noce, et al., "Limited Ferromagnetic Interactions in Monolayers of MPS_3 (M = Mn and Ni)," *Journal of Physical Chemistry C* 126 (2022): 6791–6802.

20. R. Basnet, K. M. Kotur, M. Rybak, et al., "Controlling Magnetic Exchange and Anisotropy by Nonmagnetic Ligand Substitution in Layered MPX_3 (M =Ni, Mn; X =S, Se)," *Physical Review Research* 4 (2022): 023256.

21. W. M. Linhart, M. Rybak, M. Birowska, et al., "Optical Markers of Magnetic Phase Transition in CrSBr," *Journal of Materials Chemistry C* 11 (2023): 8423–8430.

22. Z. Zhou, X. Cheng, M. Hu, J. Liu, F. Pan, and C. Song, "Crystal Design of Altermagnetism," preprint, arXiv, March 12, arXiv:2403.07396.

23. N. Dale, O. A. Ashour, M. Vila, et al., "Relativistic and Nonrelativistic Spin Splitting above and below the Fermi Level in a *g*-Wave Altermagnet," preprint, arXiv, March 17, 2026, arXiv:2411.18761.

24. A. Sakhya, M. Mondal, M. Sprague, et al., "Electronic Structure of a Layered Altermagnetic Compound $CoNb_4Se_8$," preprint, arXiv, March 20, 2025, arXiv:2503.16670.

25. See Supporting Information for structural characterization via XRD, STM images and step height analysis, magnetic susceptibility measurements, XPS core level analysis, additional ARPES and micro-ARPES data, time-reversal domain analysis with spin-ARPES, calculations of the average and impulsive heating in the ultrafast measurements, and additional DFT and ab-initio energetics.

26. H. Mandujano, S. Sheoran, Z. Yuanpeng, et al., "Evolution of Altermagnetism to Spin Density Waves in Co_xNbSe_2," *Journal of the American Chemical Society* 147 (2025): 44926–44940.

27. H. C. Mandujano, P. Y. Zavalij, A. Manjón-Sanz, H. Cao, and E. E. Rodriguez, "Coexistence of Commensurate and Incommensurate Antiferromagnetic Ground States in Co_xNbSe_2 Single Crystal," *Physical Review Materials* 9 (2025): 014403.

28. S. S. P. Parkin, E. A. Marseglia, and P. J. Brown, "Magnetic Structure of $Co_{1/3}NbS_2$ and $Co_{1/3}TaS_2$," *Journal of Physics C: Solid State Physics* 16, no. 14 (1983): 2765.

29. B. Van Laar, H. Rietveld, and D. Ijdo, "Magnetic and Crystallographic Structures of Me_xNbS_2 and Me_xTaS_2," *Journal of Solid State Chemistry* 3, no. 2 (1971): 154–160.

30. B. Edwards, O. Dowinton, A. E. Hall, et al., "Giant Valley-Zeeman Coupling in the Surface Layer of an Intercalated Transition Metal Dichalcogenide," *Nature Materials* 22, no. 4 (2023): 459–465.

31. M. Roig, A. Kreisel, Y. Yu, B. M. Andersen, and D. F. Agterberg, "Minimal Models for Altermagnetism," *Physical Review B* 110 (2024): 144412.

32. S. Reimers, L. Odenbreit, L. Šmejkal, et al., "Direct Observation of Altermagnetic Band Splitting in CrSb Thin Films," *Nature Communications* 15, no. 1 (2024): 2116.

33. X. Chen, J. Ren, Y. Zhu, et al., "Enumeration and Representation Theory of Spin Space Groups," *Physical Review X* 14 (2024): 031038.

34. Z. Xiao, J. Zhao, Y. Li, R. Shindou, and Z.-D. Song, "Spin Space Groups: Full Classification and Applications," *Physical Review X* 14 (2024): 031037.

35. Y. Jiang, Z. Song, T. Zhu, et al., "Enumeration of Spin-Space Groups: Toward a Complete Description of Symmetries of Magnetic Orders," *Physical Review X* 14 (2024): 031039.

36. T. Mitsuhashi, M. Minohara, R. Yukawa, et al., "Influence of $k_\perp$ Broadening on ARPES Spectra of the (110) and (001) Surfaces of $SrVO_3$ Films," *Physical Review B* 94 (2016): 125148.

37. V. Popescu and A. Zunger, "Extracting E versus $\vec{k}$ Effective Band Structure from Supercell Calculations on Alloys and Impurities," *Physical Review B* 85 (2012): 085201.

38. X. Zhang, Q. Liu, J.-W. Luo, A. J. Freeman, and A. Zunger, "Hidden Spin Polarization in Inversion-Symmetric Bulk Crystals," *Nature Physics* 10 (2014): 387–393.

39. J. M. Riley, F. Mazzola, M. Dendzik, et al., "Direct Observation of Spin-Polarized Bulk Bands in an Inversion-Symmetric Semiconductor," *Nature Physics* 10 (2014): 835–839.

40. J. N. Graham, T. J. Hicken, R. B. Regmi, et al., "Local Probe Evidence Supporting Altermagnetism in $Co_{1/4}NbSe_2$," *Physical Review Research* 8 (2026): 023361.

41. T. Shimizu, R. Tobise, T. Kurosawa, et al., "Critical Photoinduced Reflectivity Relaxation Dynamics in Single-Layer Bi-Based Cuprates near the Pseudogap End Point," preprint, arXiv, September 26, 2026, arXiv:2508.21298.

15214095, 0, Downloaded from https://advanced.onlinelibrary.wiley.com/doi/10.1002/adma.75367 by Universita Di Trento, Wiley Online Library on [20/10/2026]. See the Terms and Conditions (https://onlinelibrary.wiley.com/terms-and-conditions) on Wiley Online Library for rules of use; OA articles are governed by the applicable Creative Commons License

42. L. Wang, M. Ma, J. Li, et al., "Hidden Phonon-Assisted Charge Density Wave Transition in $BaFe_2Al_9$ Revealed by Ultrafast Optical Spectroscopy," preprint, arXiv, October 7, 2025, arXiv:2510.05908.

43. P. Giannozzi, S. Baroni, N. Bonini, et al., "QUANTUM ESPRESSO: A Modular and Open-Source Software Project for Quantum Simulations of Materials," *Journal of Physics: Condensed Matter* 21, no. 39 (2009): 395502.

44. P. Giannozzi, O. Andreussi, T. Brumme, et al., "Advanced Capabilities for Materials Modelling With QUANTUM ESPRESSO," *Journal of Physics: Condensed Matter* 29, no. 46 (2017): 465901.

45. K. F. Garrity, J. W. Bennett, K. M. Rabe, and D. Vanderbilt, "Pseudopotentials for High-Throughput DFT Calculations," *Computational Materials Science* 81 (2014): 446–452.

46. J. P. Perdew, K. Burke, and M. Ernzerhof, "Generalized Gradient Approximation Made Simple," *Physical Review Letters* 77 (1996): 3865–3868.

47. M. Methfessel and A. T. Paxton, "High-Precision Sampling for Brillouin-Zone Integration in Metals," *Physical Review B* 40 (1989): 3616–3621.

48. D. Pacilè, C. Cardoso, G. Avvisati, et al., "Narrowing of d Bands of FeCo Layers Intercalated under Graphene," *Applied Physics Letters* 118, no. 12 (2021): 121602.

Supporting Information

Additional supporting information can be found online in the Supporting Information section.

Supporting File: adma75367-sup-0001-SuppMat.pdf.

15214095, 0, Downloaded from https://advanced.onlinelibrary.wiley.com/doi/10.1002/adma.75367 by Universita Di Trento, Wiley Online Library on [20/10/2026]. See the Terms and Conditions (https://onlinelibrary.wiley.com/terms-and-conditions) on Wiley Online Library for rules of use; OA articles are governed by the applicable Creative Commons License